Optimum Boundary Inductance Control Concerning Limited PF for a DCM Boost PFC Converter

Kai Yao, *Member, IEEE*, Lei Li, Huanqi Tang, Chunyan Mao, and Kaili Chen

***Abstract*—The discontinuous conduction mode boost power factor correction converter features zero-current turn-ON for the switch, no reverse recovery in diode, and constant frequency operation. With traditional constant duty ratio control, the power transfer in each switching cycle exhibits great difference during a half-line cycle. Consequently, the peak and root mean square values of the inductor current are large, the same goes for the switch and diode. This increases not only the current stress of the power components but also the conduction and switching turn-OFF loss, and lowers the efficiency of the converter. Introducing third and fifth harmonics into the input current and varying the duty cycle correspondingly can reduce the aforementioned power transfer difference, and provide huge space for the increment of boundary inductance as well. An optimum boundary inductance control concerning limited power factor (PF) is proposed in this paper. For the maximum boundary inductance of the converter within wide input voltage range, the optimum harmonics amounts are analyzed and figured out. The proposed method brings about efficiency improvement, output voltage ripple reduction, and PF increase as well, especially at high input voltages. A prototype has been built and the experimental results are presented to show the validity of the scheme.**

***Index Terms*—Boost, discontinuous conduction mode (DCM), limited power factor (PF), optimum boundary inductance (OBI), power factor correction (PFC).**

I. Introduction

FOR THE improvement of grid power quality and the reduction of line current distortion, power factor correction (PFC) is necessary in ac–dc conversion. Many topologies and control methods of PFC have been put forward for low total harmonics distortion and high power factor (PF) [1]–[4]. Discontinuous conduction mode (DCM) boost PFC converters are widely employed in low-to-medium power applications because of its several merits [5]–[11].

Manuscript received November 30, 2018; revised March 4, 2019; accepted April 5, 2019. Date of publication April 18, 2019; date of current version October 18, 2019. This work was supported in part by the National Natural Science Foundation of China under Grant 51677091, in part by the Excellent Youth Fund Project of Jiangsu Natural Science Foundation under Grant BK20160086, in part by the Six Talents Peak Project of Jiangsu Province under Grant XNY-033, and in part by the Fundamental Research Funds for the Central Universities under Grant 30918011331. Recommended for publication by Associate Editor M. Ponce-Silva. *(Corresponding author: Kai Yao.)*

The authors are with the School of Automation, Nanjing University of Science and Technology, Nanjing 210094, China (e-mail: yaokai@njust.edu.cn; 116110001008@njust.edu.cn; 18090015107@163.com; 1095859615@qq.com; 617921503@qq.com).

Color versions of one or more of the figures in this paper are available online at http://ieeexplore.ieee.org.

Digital Object Identifier 10.1109/TPEL.2019.2912324

The work in [5] provides a systematic analysis of the upper and lower limits to output voltage and power in a DCM boost PFC converter regarding the input current distortion. A digital signal processor (DSP) implementation and step-by-step design procedure is presented in [6] for the control of a DCM boost PFC converter in universal line-voltage applications. The research in [7] gives a comprehensive design and optimization of a high-power-density single-phase boost PFC converter. In [8], a variable-duty-cycle control is proposed to improve the PF to nearly unity under universal input voltages. A direct ac–dc boost converter at DCM is proposed in [9] for efficient and optimum energy harvesting from low-voltage microgenerators. The study in [10] builds a model for the PFC converter operation mode prediction under practical circumstances, based on which analysis of the output voltage and power limitations is provided. The work in [11] presents a variable duty cycle control technique for improving PF of quadratic DCM–DCM boost PFC converter.

When PFC converters designed for operation in continuous conduction mode (CCM) at full power are operated at reduced load, operation in DCM occurs in a zone that is close to the crossover of the line voltage. This zone will gradually expand with decreasing load to finally encompass the entire line cycle, resulting in significant input current distortion. The work in [12] proposes a mixed-mode input current sensor-less predictive current control at constant but two different switching frequencies for a single-phase boost PFC converter. A digitally controlled boost PFC converter is introduced in [13], where a dedicated control algorithm consisting of sample correction and duty-ratio feed-forward is proposed. The study in [14] gives analysis about the source of input-current distortion of CCM boost PFC converters operated in DCM and a solution of several snubber types is evaluated. In [15], a predictive current control law based on a DCM detection circuit is modified to improve current shaping and adaptive switching and adaptive frequency control techniques are introduced to reduce switching losses. A simple digital DCM control scheme which introduces minimal changes to the CCM average current control structure and can be achieved in a single clock cycle is proposed in [16]. A robust autotuning technique to achieve the desired crossover frequencies and phase margins as well as a precise estimation of the filter inductance and capacitance is presented in [17]. In [18], a DCM detection method is proposed using the added capabilities of a DSP with integrated comparators and a simple digital controller architecture that changes its compensator to suit DCM or CCM operation is introduced. In [19], the characteristics of the common-mode and differential-mode noise of the converter are

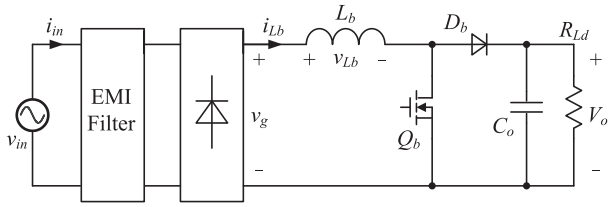

Fig. 1. Main circuit of boost PFC converter.

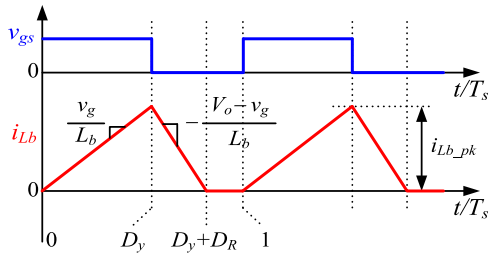

Fig. 2. Inductor current waveform in switching cycles.

analyzed for average-current-controlled boost PFC converters operating in both CCM and DCM under different input voltage and load conditions. For future on-chip implementation, a high-frequency boost PFC rectifier with small form-factor and a digital mix-conduction-mode controller for 1 MHz operation without the need of average current sensing is proposed in [20]. A digital phase leading filter current compensation technique for a CCM boost PFC to improve PF in high line voltage and light load conditions is proposed in [21].

Constant duty ratio control (CDC) of DCM boost PFC converters leads to huge difference of power conversion in each switching period during an input cycle. The resultant high peak and root mean square (RMS) currents of power components yield negative influence on the current stress and the conversion efficiency. In order to increase the critical inductance as much as possible and the efficiency of the converter, an optimum boundary inductance (OBI) control concerning limited PF (OBIP) is put forward. The basic relationship between the electrical parameters of DCM boost PFC converter is listed in Section II. In Section III, the OBI control is proposed and the optimum third and fifth harmonics amounts are figured out. Section IV gives the comparison between OBIP and CDC in the aspect of the PF, the input current, the RMS and peak current of the inductor, and the output voltage ripple. The control circuit and the experimental results are presented in Section V. Section VI summarizes the paper.

II. Working Principle of DCM Boost PFC Converter

Fig. 1 shows the main circuit of a boost PFC converter. When the converter operates at DCM, the inductor current waveforms in switching cycles and a half-line cycle are shown in Figs. 2 and 3, respectively.

The detailed derivation process has been given in [8], where the input voltage, the rectified voltage, the input current, the peak and the RMS value of the inductor current, the relationship

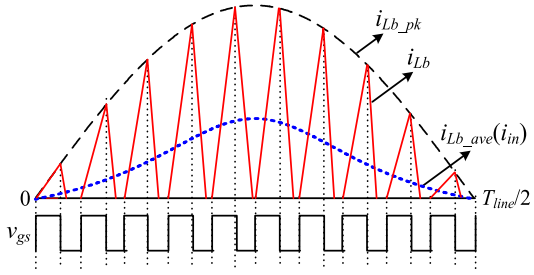

Fig. 3. Inductor current waveform in a half-line cycle.

between the on-duty-cycle and the off-duty-cycle corresponding to the falling period of the inductor current are listed in (1)–(5). With CDC, the duty cycle, the PF and the critical inductance are expressed in (6)–(8)

$$v_{\text{in}} = v_g = V_m \sin \omega t \tag{1}$$

$$i_{\text{in}} = \frac{V_m D_y^2}{2 L_b f_s} \frac{\sin \omega t}{1 - \alpha \sin \omega t} \tag{2}$$

$$i_{Lb\_pk} = \frac{D_y V_m \sin \omega t}{L_b f_s} \tag{3}$$

$$I_{Lb\_\text{rms}} = \frac{V_m T_s}{L_b} \sqrt{\frac{1}{\pi} \int_0^{\pi} \frac{D_y^3 \sin^2 \omega t}{3\,(1 - \alpha \sin \omega t)} d\omega t} \tag{4}$$

$$D_R = \frac{\alpha \sin \omega t}{1 - \alpha \sin \omega t} D_y \tag{5}$$

$$D_y = \frac{1}{V_m} \sqrt{\frac{2\pi L_b f_s P_o}{\int_0^{\pi} \frac{\sin^2 \omega t}{1 - \alpha \sin \omega t} d\omega t}} \tag{6}$$

$$\text{PF} = \frac{\sqrt{\frac{2}{\pi}} \int_0^{\pi} \frac{\sin^2 \omega t}{1 - \alpha \sin \omega t} d\omega t}{\sqrt{\int_0^{\pi} \frac{\sin^2 \omega t}{(1 - \alpha \sin \omega t)^2} d\omega t}} \tag{7}$$

$$L_{b1} = \frac{V_m^2 (1 - \alpha)^2}{2\pi f_s P_o} \int_0^{\pi} \frac{\sin^2 \omega t}{1 - \alpha \sin \omega t} d\omega t \tag{8}$$

where V_m and ω are the amplitude and angular frequency of the input voltage, V_o is the output voltage, $\alpha = V_m / V_o$, and $0 \le \omega t \le \pi$.

Using (8) and the specifications of the converter given in Table I in Section V, we can plot Fig. 4. By Fourier analysis, the input current harmonics can be obtained, and Fig. 5 exhibits the ratio of the third, fifth, and seventh RMS values to the input power. It should be noted that the negative value means that the corresponding harmonic has a phase difference of π with respect to the fundamental component.

III. Optimum Harmonics for Maximum Boundary Inductance

Referring Fig. 2 and (5), (6), the discontinuous degree of the inductor current is defined as $1 - D_y - D_R$ for the sake of analysis. For DCM boost PFC converter with CDC, during a

TABLE I
SPECIFICATIONS OF THE PROTOTYPE

input voltage	output voltage	output power	switching frequency
v_{in} =90 ~ 264 VAC / 50 Hz	V_o = 400 VDC	P_o = 120 W	f_s = 100 kHz

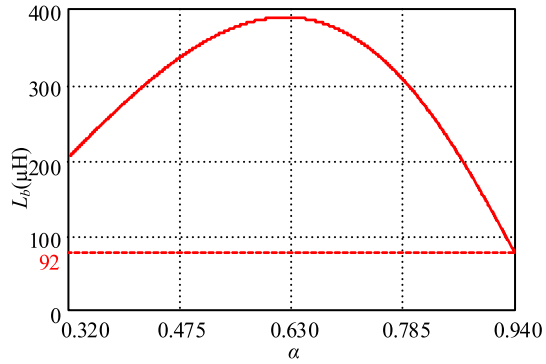

Fig. 4. Critical inductance with CDC.

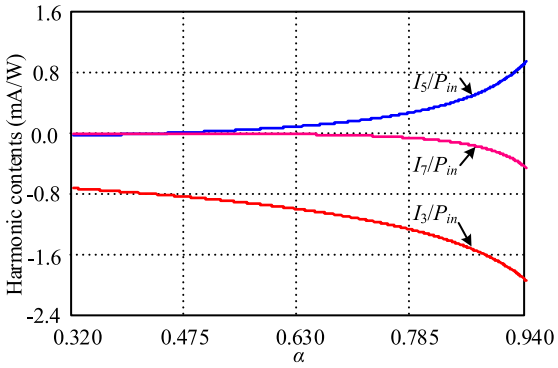

Fig. 5. Harmonic contents per-Watt with CDC.

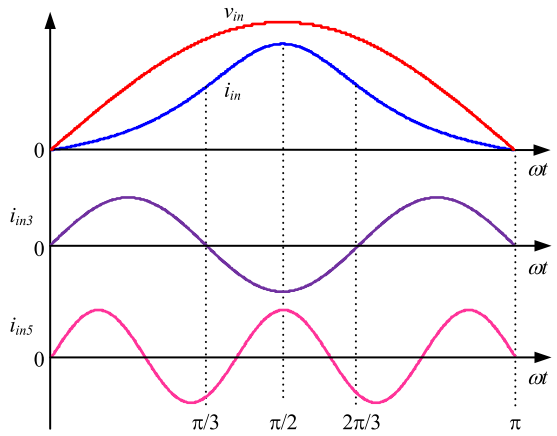

Fig. 6. Waveforms of the input current with CDC, third and fifth harmonics.

half-line cycle of a certain input voltage, the discontinuous degree of the inductor current decreases within [0, π/2] and increases with [π/2, π]. This also explains why the critical inductance occurs at $V_{\text{in\_RMS}} = 264$ V and $\omega t = \pi/2$, which, actually, is the only point where the inductor current is in critical conduction mode, within [0, π] and during 90–264 Vac. In addition, the aforementioned analysis indicates that, the input current mainly contains the third harmonics with a phase difference of π in regard to the fundamental one. For the convenience of explanation, the input current with CDC, and the third together with the fifth harmonic in phase with the fundamental one are plotted in Fig. 6.

Let us make the following assumption. Introducing a certain amount of i_{in3} into the input current i_{in} will increases its value within [0, π/3] and [2π/3, π], and decrease its value within [π/3, 2π/3]. As the input current is the average value of the inductor current in a switching cycle, the duty cycle should be adjusted accordingly, if the inductance is kept the same as that with CDC. Or rather, instead of a constant value within a half-line cycle, the duty cycle should be increased within [0, π/3] and [2π/3, π], and decreased within [π/3, 2π/3]. Thus, the off-duty-cycle will increase and decrease in proportion. It is not difficult to find that, the discontinuous degree of the inductor current will become lower within [0, π/3] and [2π/3, π], and higher within [π/3, 2π/3] correspondingly, which, fortunately, can provide space for us to adopt an inductance higher than the original one with CDC.

From the variation rule of the third harmonic in Fig. 6, it is not difficult to imagine that if the original input current is introduced into some third harmonic, the discontinuous degree of the inductor current within [0, π/6] and [5π/6, π] is always higher than that within [π/6, 5π/6]. In fact, with the increase of the third harmonic amplitude, the electrical angle at which the discontinuous degree of the inductor current is the lowest will move gradually from π/2 to π/6 and 5π/6. Interestingly, at π/3 and 2π/3, i.e., the exact middle points between π/2 and π/6 as well as 5π/6, the third harmonic values are always 0, no matter how much its amplitude is. In other words, at π/3 and 2π/3, the instantaneous value of the original input current with CDC cannot be changed. As a result, the room for the inductance increment may be constrained at these two angles. Obviously, the fifth harmonic can remove this restriction. Therefore, we can also take this into consideration for the possible further increase of the inductance.

A. *Derivation of Optimum Third and Fifth Harmonics*

For the OBI control, the input current is defined as

$$\begin{aligned} i_{\text{in}} &= I_1 \left(\sin \omega t + I_3^* \sin 3\omega t + I_5^* \sin 5\omega t\right) \\ &= \frac{2P_o}{V_m} \left(\sin \omega t + I_3^* \sin 3\omega t + I_5^* \sin 5\omega t\right) \end{aligned} \tag{9}$$

where I_1 is the amplitude of the fundamental component, I_3^* and I_5^* are the normalized amplitude of the third and fifth harmonics,

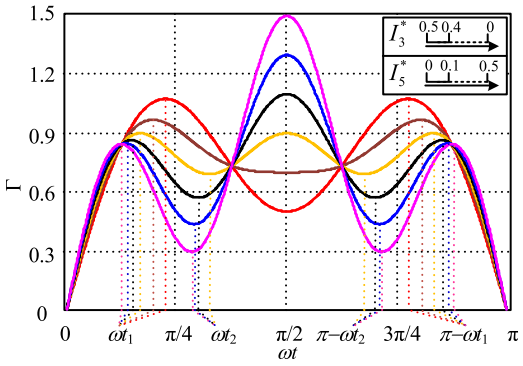

Fig. 7. Group of lines with different I_3^* and I_5^*.

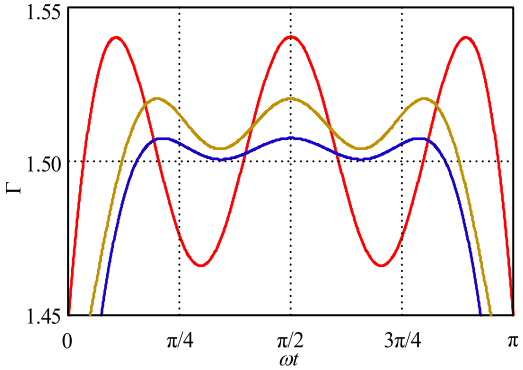

Fig. 8. Different groups of I_3^* and I_5^* achieving same value at ωt_1 and $\pi/2$.

respectively. The combination of (2) and (9) yields the duty cycle as (10) as shown bottom of the page.

Substituting (10) into (5) combining $D_y + D_R \le 1$ and defining $\sin \omega t = x$ results in the critical inductance

$$L_b \le \frac{V_m^2}{4 f_s P_o} \frac{1-\alpha x}{1 + I_3^* (3 - 4x^2) + I_5^* (5 - 20x^2 + 16x^4)}. \tag{11}$$

For simplicity, let us omit the constant coefficients and exchange the numerator and denominator as follows:

$$\Gamma(x) = \frac{1 + I_3^* (3 - 4x^2) + I_5^* (5 - 20x^2 + 16x^4)}{1 - \alpha x}. \tag{12}$$

A group of curves for (12) are drawn in Fig. 7, with I_3^* decreasing and I_5^* increasing from the top to the bottom. It can be noticed that there may be three cases about extreme points, corresponding to the angle of $\pi/2$, ωt_1, and $\pi - \omega t_1$, ωt_2, and $\pi - \omega t_2$, respectively. Furthermore, the local peak values at ωt_1 and $\pi/2$ change toward the opposite direction.

Obviously, the optimum situation is that the two values equal. Interestingly, many groups of I_3^* and I_5^* can achieve this situation, as shown in Fig. 8.

First, we come to the solution of x_1.

Differentiating (12) with x and setting it equal to 0 leads to

$$x^4 - \frac{4I_5^*}{3\alpha} x^3 - \frac{1}{12}\left(5 + \frac{I_3^*}{I_5^*}\right) x^2 + \frac{1}{6\alpha}\left(5 + \frac{I_3^*}{I_5^*}\right) x - \frac{1}{48}\left(5 + \frac{3I_3^*}{I_5^*} + \frac{1}{I_5^*}\right) = 0. \tag{13}$$

For simplicity, the following symbols are defined:

$$b = -\frac{4I_5^*}{3\alpha} \quad c = -\frac{1}{12}\left(5 + \frac{I_3^*}{I_5^*}\right) \quad d = \frac{1}{6\alpha}\left(5 + \frac{I_3^*}{I_5^*}\right) \quad e = -\frac{1}{48}\left(5 + \frac{3I_3^*}{I_5^*} + \frac{1}{I_5^*}\right) \tag{14a}$$

$$A = 8 \quad B = -4c \quad C = 2bd - 8e \quad D = e\left(4c - b^2\right) - d^2 \tag{14b}$$

$$p = \frac{C}{A} - \frac{B^2}{3A^2} \quad q = \frac{2B^3}{27A^3} - \frac{BC}{3A^2} + \frac{D}{A} \tag{14c}$$

$$y = \sqrt[3]{-\frac{q}{2} + \sqrt{\left(\frac{q}{2}\right)^2 + \left(\frac{p}{3}\right)^3}} + \sqrt[3]{-\frac{q}{2} - \sqrt{\left(\frac{q}{2}\right)^2 + \left(\frac{p}{3}\right)^3}} - \frac{B}{3A}. \tag{14d}$$

Then the solution of (13) is formulated as

$$x_1 = \frac{1}{4}\left[\sqrt{\left(b + \sqrt{8y + b^2 - 4c}\right)^2 - 16\left(y + \frac{by - d}{\sqrt{8y + b^2 - 4c}}\right)} - \left(b + \sqrt{8y + b^2 - 4c}\right)\right]. \tag{15}$$

Equation (15) gives the relationship between the local peak point and I_3^*, I_5^*, α. Now, the problem is how to determine the optimum I_3^* and I_5^* for the maximum inductance L, i.e., the minimum value Γ.

Defining the Lagrange's conditional extremum function as follows:

$$F(I_3^*, I_5^*) = \Gamma\left[\sin\left(\frac{\pi}{2}\right)\right] + k\left\{\Gamma(x_1) - \Gamma\left[\sin\left(\frac{\pi}{2}\right)\right]\right\} = \frac{1 - I_3^* + I_5^*}{1 - \alpha} + k\left[\Gamma(x_1) - \frac{1 - I_3^* + I_5^*}{1 - \alpha}\right] \tag{16}$$

where k is an auxiliary parameter.

Theoretically, the optimum values $I_{3\_\mathrm{OBI}}^*$ and $I_{5\_\mathrm{OBI}}^*$ can be figured out from the following equations and expressed as a function of α. Nonetheless, the equations are too complex to be solved directly. For a specific α, $I_{3\_\mathrm{OBI}}^*$, and $I_{5\_\mathrm{OBI}}^*$ can

$$D_y = \frac{2\sqrt{L_b f_s P_o}}{V_m} \cdot \sqrt{(1 - \alpha \sin \omega t)\left[1 + I_3^*\left(3 - 4\sin^2 \omega t\right) + I_5^*\left(5 - 20\sin^2 \omega t + 16\sin^4 \omega t\right)\right]}. \tag{10}$$

TABLE II
MAIN COMPONENTS OF THE PROTOTYPE

input rectifier bridge *RB*	power switch Q_b	boost diode D_b	control IC
GBU406 (600 V, 4 A)	FCI11N60 (600 V, 11 A)	STTH8L06D (600 V, 8 A)	DSP28335
boost inductor	input filter inductor	input filter capacitor	output filter capacitor
80 μH (CDC), 230 μH (OBIP)	L_{in}= 230 μH	C_{in}= 0.47 μF	C_o = 220 μF

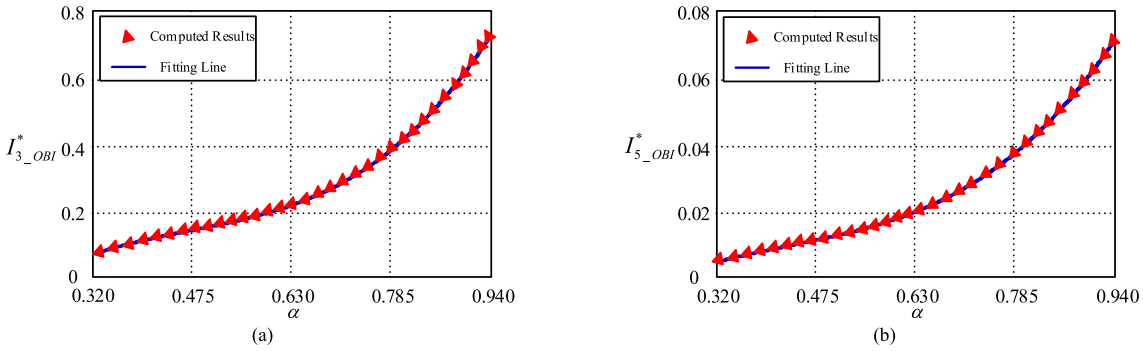

Fig. 9. Fitted curves of the optimum harmonic. (a) Third harmonic. (b) Fifth harmonic.

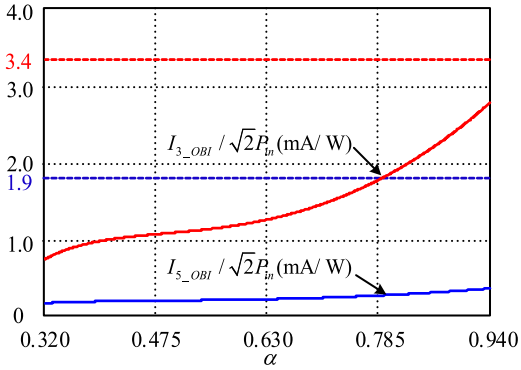

Fig. 10. Optimum harmonics and their limits.

be obtained by mathematical tool and software, as listed in Table III in the Appendix and depicted in Fig. 9.

$$\begin{cases} \dfrac{\partial F\left(I_3^*, I_5^*\right)}{\partial I_3^*} = 0 \\ \dfrac{\partial F\left(I_3^*, I_5^*\right)}{\partial I_5^*} = 0 \\ \dfrac{\partial F\left(I_3^*, I_5^*\right)}{\partial k} = 0 \end{cases}. \tag{17}$$

Through mathematical analysis, we finally acquire a fitted function as follows. The fitted curve overlaps the computed one very well, as shown in Fig. 9

$$I^*_{3\_\mathrm{OBI}} = 3.985\alpha^3 - 5.569\alpha^2 + 2.996\alpha - 0.459 \tag{18a}$$

$$I^*_{5\_\mathrm{OBI}} = 0.355\alpha^3 - 0.492\alpha^2 + 0.265\alpha - 0.041. \tag{18b}$$

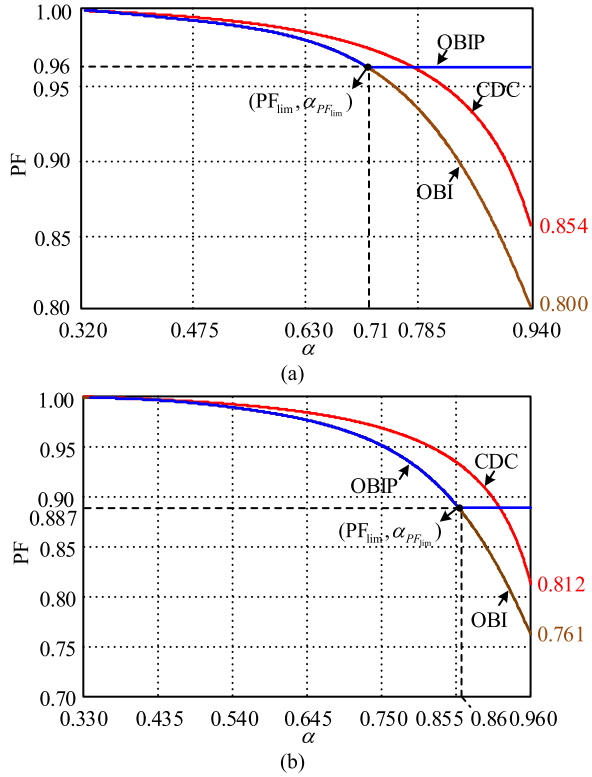

Fig. 11. PF curves with different control. (a) At $V_o = 400$ V. (b) At $V_o = 390$ V.

The ratio of the third and fifth harmonics to the input power can be calculated as

$$\frac{I_{3,5}}{P_{\mathrm{in}}} = \frac{I_{3,5}}{I_1 \cdot V_m/\sqrt{2}} = \frac{I^*_{3,5}}{V_m/\sqrt{2}}. \tag{19}$$

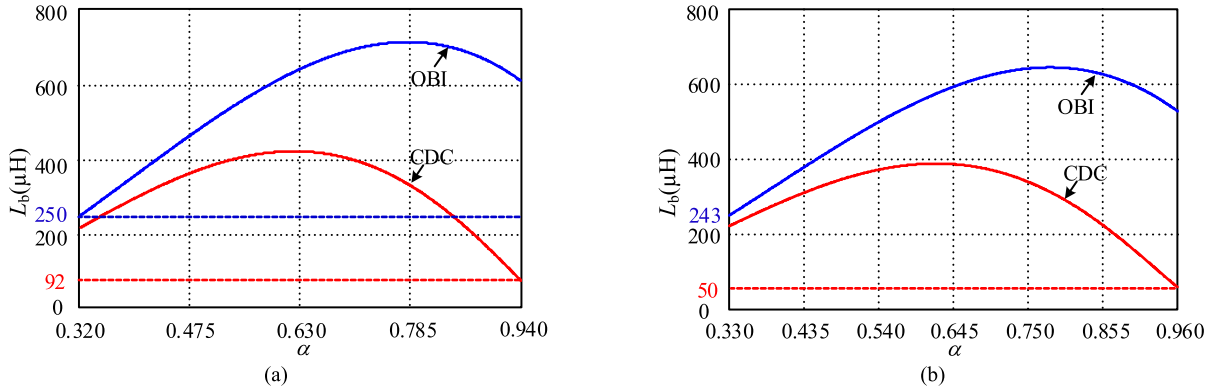

Fig. 12. Critical inductance curve for CDC and OBI with 120 W and 100 kHz. (a) At $V_o = 400$ V. (b) At $V_o = 390$ V.

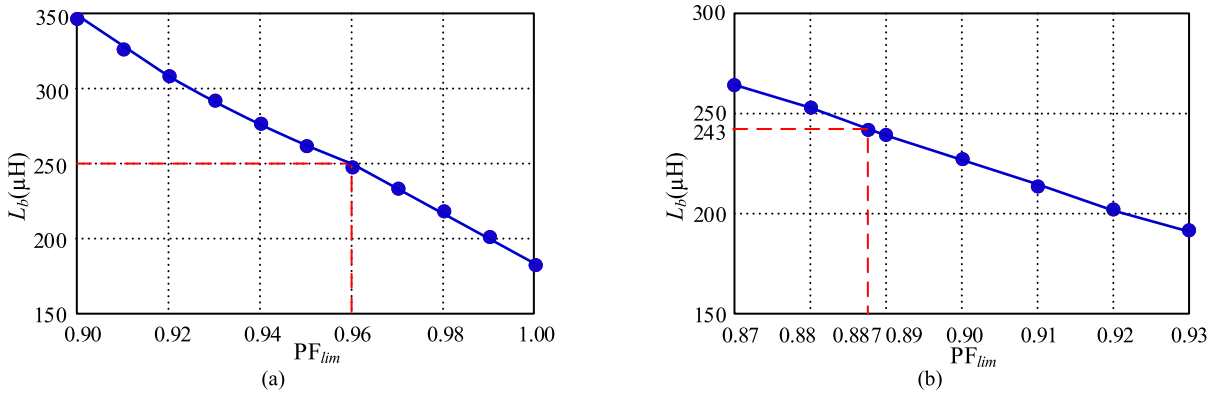

Fig. 13. Achievable maximum inductance versus $\mathrm{PF_{lim}}$ with 264 Vac, 120 W, and 100 kHz. (a) At $V_o = 400$ V. (b) At $V_o = 390$ V.

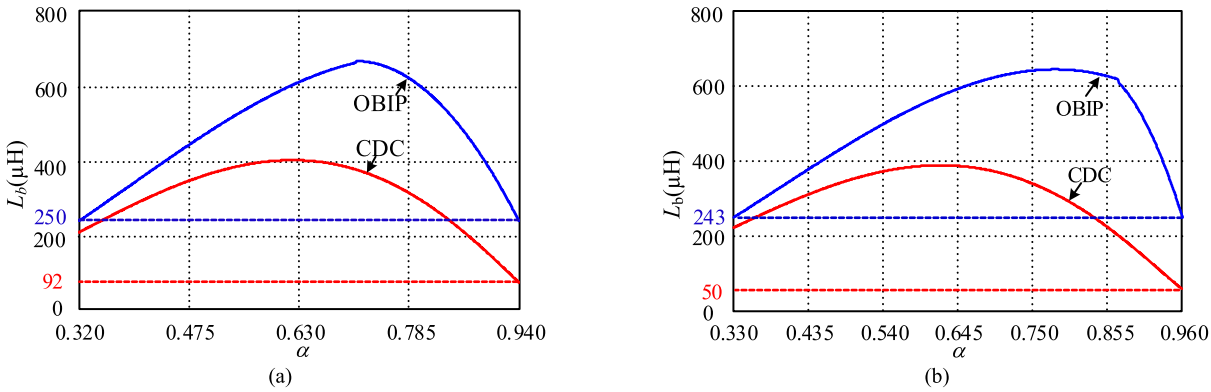

Fig. 14. Critical inductance curve for CDC and OBIP with 120 W and 100 kHz. (a) At $V_o = 400$ V. (b) At $V_o = 390$ V.

Based on (18) and (19), we can draw Fig. 10, where 3.4 mA/W and 1.9 mA/W are the limits of third and fifth harmonics from IEC61000-3-2 Class D. It is clear that the harmonics meet the standard requirements.

B. Compromise Scheme Concerning PF

Fig. 11 can be plotted from (7) and (18). Substituting x = 1 and (18) into (11), and combining with the specifications in Section V, we can get Fig. 12. The figures explicitly demonstrate that, compared with CDC, the PF is lowered and the critical inductance is increased with the OBI control, especially at high input voltages. In other words, the great increment of inductance at high input voltages is achieved at the cost of PF. Unfortunately, such a sacrifice does not make a sense, for the inductance should be selected at $\alpha = 0.32$ to satisfy the wide input voltage range. Therefore, a scheme of OBIP is put forward here, which can improve the PF and keep the inductance no less than 250 μH at high input voltages.

It is easy to find that a $\mathrm{PF_{lim}}$ corresponds to an $\alpha_{\mathrm{PF_{lim}}}$ in Fig. 11. During [0.32, $\alpha_{\mathrm{PF_{lim}}}$], the optimum I_3^* and I_5^* for OBIP is the same as that for OBI. For the rest period [$\alpha_{\mathrm{PF_{lim}}}$, 0.94], a systematic analysis reveals that it can be divided into two parts, and the critical inductance is got at x_1 expressed in (15) for the first part and sin (π/2) for the second part.

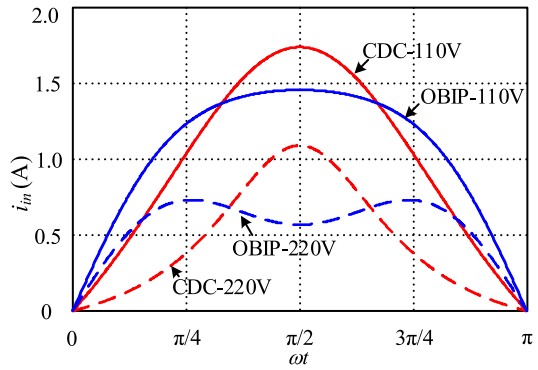

Fig. 15. Input current in a half-cycle.

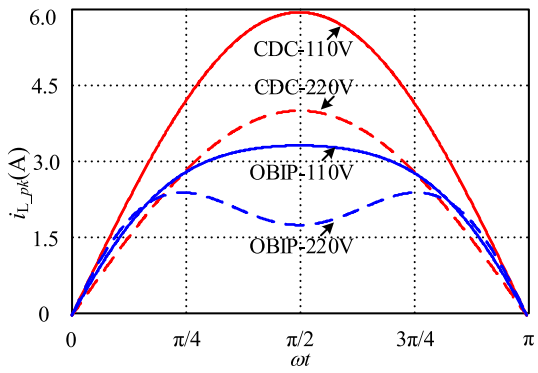

Fig. 16. Peak current of the inductor.

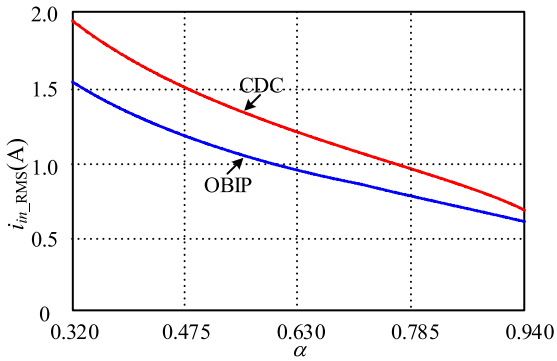

Fig. 17. RMS current of the inductor.

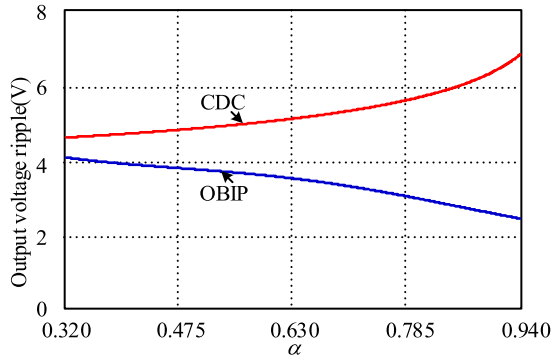

Fig. 18. Output voltage ripple.

For the period $[\alpha_{\mathrm{PF_{lim}}}, 0.94]$, I_3^* and I_5^* should satisfy

$$\frac{1}{\sqrt{1+I_3^{*2}+I_5^{*2}}} = \mathrm{PF_{lim}}. \tag{20}$$

Thus, the fifth harmonic is expressed as

$$I_5^* = \sqrt{\frac{1}{\mathrm{PF_{lim}^2}} - 1 - I_3^{*2}}. \tag{21}$$

The substitution of (21) and (15) into (12) leads to a function consisting of I_3^*, α, and $\mathrm{PF_{lim}}$. Differentiating the function with I_3^* and setting it equal to 0 results in the optimum $I_{3\_\mathrm{OBIP}}^*$. Correspondingly, the optimum $I_{5\_\mathrm{OBIP}}^*$ can be got from (21). This is for the first part.

Substituting $I_{3\_\mathrm{OBIP}}^*$ and $I_{5\_\mathrm{OBIP}}^*$ into (15) yields a function regarding α and $\mathrm{PF_{lim}}$. Defining this function as 1, we will obtain the demarcation point α_d between the first and the second part.

Replacing x and I_5^* in (12) with 1 and (21) respectively, we have

$$\Gamma\left[\sin\left(\frac{\pi}{2}\right)\right] = \frac{1 - I_3^* + \sqrt{\frac{1}{\mathrm{PF_{lim}^2}} - 1 - I_3^{*2}}}{1-\alpha}. \tag{22}$$

Obviously, the optimum $I_{3\_\mathrm{OBIP}}^*$ is $\sqrt{\frac{1}{\mathrm{PF_{lim}^2}} - 1}$. This is for the second part.

In summary, Table IV can be illustrated from the analysis above. Specifically, at 264 Vac, the achievable highest PF is 0.96 lest the inductance is less than 250 μH, which can also be seen from Fig. 13. Ensuring PF $\geq$ 0.96, we can obtain the fitted expression of $I_{3\_\mathrm{OBIP}}^*$ and $I_{5\_\mathrm{OBIP}}^*$ for the three input voltage ranges

$$I_{3\_\mathrm{OBIP}}^* = \begin{cases} 3.985\alpha^3 - 5.569\alpha^2 + 2.996\alpha - 0.459 & 0.32 \leq \alpha \leq 0.71 \\ -0.6064\alpha^2 + 0.9141\alpha - 0.0529 & 0.71 < \alpha \leq 0.76 \\ 0.2917 & 0.76 < \alpha \leq 0.94 \end{cases} \tag{23a}$$

$$I_{5\_\mathrm{OBIP}}^* = \begin{cases} 0.355\alpha^3 - 0.492\alpha^2 + 0.265\alpha - 0.041 & 0.32 \leq \alpha \leq 0.71 \\ 1.103\alpha^2 - 2.1961\alpha + 1.0157 & 0.71 < \alpha \leq 0.76 \\ 0 & 0.76 < \alpha \leq 0.94 \end{cases}. \tag{23b}$$

Correspondingly, the critical inductance curve is obtained, as shown in Fig. 14.

Furthermore, we have analyzed different cases regarding different output voltage, switching frequency, and output power. The results are shown in Figs. 11(b)–14(b) and Tables V–VII in the Appendix. The following conclusion could be obtained. For a given output power and switching frequency, the output voltage value has a large impact on the PF of the converter, regardless of the control. Interestingly, as for the influence of

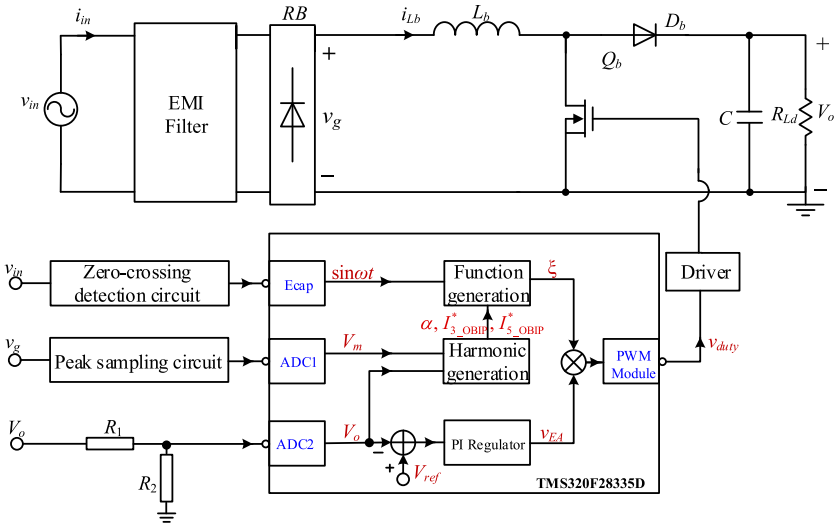

Fig. 19. Control diagram.

the output voltage value on the critical inductance, the answer is high for CDC and low for OBIP. The reasons are explained as follows. As shown in Fig. 12, for CDC, the critical mode is only achieved at the line angle of $\pi/2$ under 264 Vac, and the peak voltage value is 373 V, whose difference between 400 and 390 V is 27 and 17 V, respectively, leading to great change of the inductor current falling rate and the critical inductance as well. While for OBIP, the critical inductance is decided by the operation under 90 Vac, whose difference between 400 and 390 V is huge, and the 10 V change of the output voltage does not have great influence on the inductor current falling rate and the critical inductance. In addition, the double power or switching frequency results in half of the critical inductance.

IV. Performance Comparison

A. Power Factor

The utilization of (23) and the specifications of the converter bring about the PF of OBIP, which is plotted in Fig. 11. Compared with that of CDC, the PF of OBIP is slightly sacrificed at low input voltages and greatly improved at high input voltages. Specifically, OBIP and CDC achieve nearly the same PF at the nominal input voltage of 110 and 220 Vac.

B. Input Current and Peak and RMS Current of Inductor

Substituting (6), (10), (23) into (2), (3), (4) and combining the specifications of the converter, we can acquire the input current, the peak, and RMS current of the inductor for CDC and OBIP, respectively. Figs. 15–17 present the corresponding curves. As can be seen from Fig. 15, the input currents are not sinusoidal and the distortion pattern of CDC and OBIP is different. Fig. 16 demonstrates that OBIP achieves a lower value around $\pi/2$ and a higher value around 0 and π, compared with CDC. Fig. 17 shows that a lower RMS value of the inductor current is realized by OBIP, especially at low input voltages.

C. Output Voltage Ripple

The output voltage ripple can be formulated as

$$\Delta V_o = \frac{2}{\omega C_o V_o}\int_0^{\omega t_c}(P_o - v_{\rm in} i_{\rm in})\,d\omega t \tag{24}$$

where ωt_c is time instant when the instantaneous input power equals the output power.

The substitution of (2), (6), (9), (23) into (24) yields the ripple of the converter with CDC and OBIP, respectively, as depicted in Fig. 18. The ripple with OBIP is reduced, especially at high input voltages.

V. Experimental Verification

For the verification of the proposed control scheme, a prototype has been built and tested in the laboratory. The specifications and the main components of the prototype are shown in Tables I and II.

The control implementation is demonstrated in Fig. 19, where a DSP is adopted, for (10) is complex to be realized in an analog way. The output voltage V_o and the peak value of the rectified input voltage V_m are sent into DSP by analog-to-digital converter (ADC) module. In consequence, $\alpha = V_m/V_o$ is identified and $I^*_{3\_\rm OBIP}$, $I^*_{5\_\rm OBIP}$ are generated by the software based on (23). Meanwhile, the sampled output voltage is compared with the reference voltage $V_{\rm ref}$ and regulated by the error amplifier, and the output is v_{EA}. Through zero-crossing detection circuit, an interrupt will be triggered when the input voltage crosses zero. In this way, a sinusoidal function with the same initial phase and frequency as those of the input voltage is generated in DSP Then,

$$\xi(\omega t) = \sqrt{\begin{aligned}&(1-\alpha\sin\omega t)[1 + I^*_{3\_OBIP}(3 - 4\sin^2\omega t)\\&+ I^*_{5\_OBIP}(5 - 20\sin^2\omega t + 16\sin^4\omega t)]\end{aligned}},$$

a part of (10), can be produced by the function generation software. Finally, v_{EA} and ξ are multiplied and interacted with the triangle waveforms. Therefore, the variable duty cycle expressed in (10) is achieved.

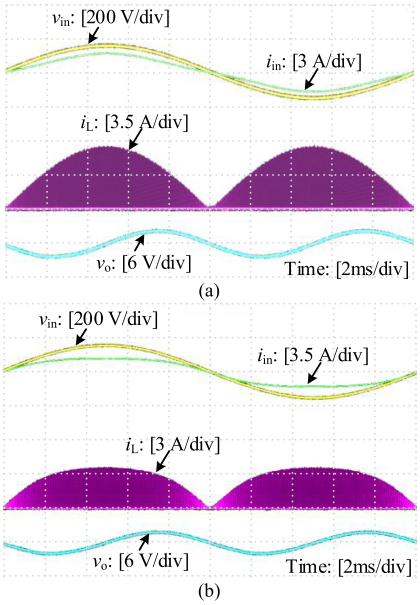

Fig. 20. Experimental waveforms in a line cycle at 110 Vac. (a) With CDC. (b) With OBIP.

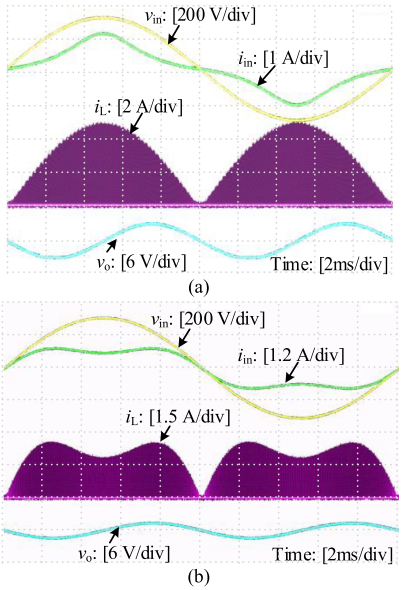

Fig. 21. Experimental waveforms in a line cycle at 220 Vac. (a) With CDC. (b) With OBIP.

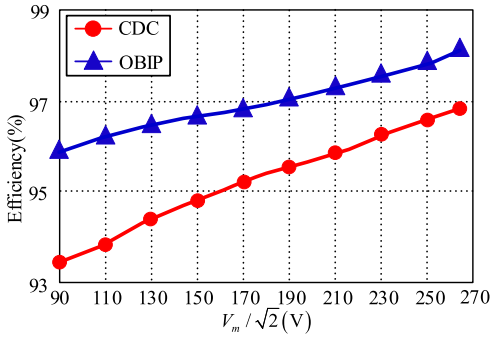

Fig. 22. Experimental results of efficiency.

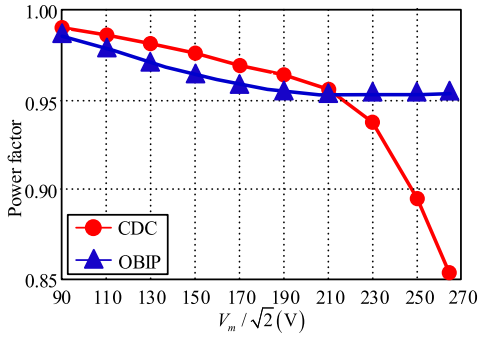

Fig. 23. Experimental results of PF.

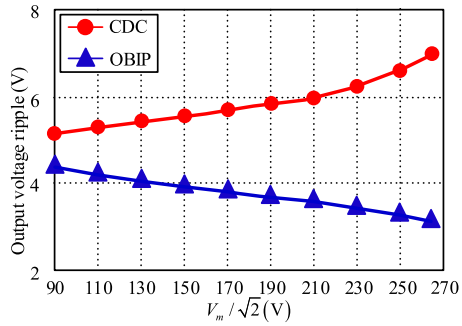

Fig. 24. Experimental results of output voltage ripple.

The experimental waveforms of the input voltage, input current, inductor current, and output voltage in a line cycle are displayed in Figs. 20 and 21, for the converter with CDC and OBIP operated at 110 and 220 Vac respectively. Obviously, because of the changed duty cycle, the shape of the input current and the peak envelope of the inductor current with OBIP are different from those with CDC.

Fig. 22 shows the measured efficiency and OBIP achieves a higher efficiency than that with CDC. The reason is explained as follows. Figs. 16, 20, and 21 demonstrate that, at low input voltages, the peak value of the switch current, i.e., the peak value of the inductor current, is greatly reduced at any line angle in a half-line cycle of $[0, \pi]$, while, at high input voltages, the value decreases around $\pi/2$ and increases around 0 and π. Thus, the switching turn-OFF loss is reduced, especially at low input voltages. Moreover, the conduction loss of the power components is reduced, as can be inferred from Fig. 17, where the inductor current's RMS value with OBIP is lower than that with CDC.

Fig. 23 indicates that the input PF with OBIP is slightly lower than that with CDC during low input voltage range. During high input voltage range, the PF with CDC decreases dramatically when the input voltage increases. However, OBIP can achieve a stable PF higher than 0.95.

The tested output voltage ripple is exhibited in Fig. 24, where we can find that OBIP brings about a lower ripple value, especially at high input voltages.

VI. Conclusion

This paper proposes an OBIP for DCM boost PFC converters. The influence of the current harmonics on the critical inductance is mathematically analyzed in detail and the optimum third and fifth harmonics amounts are discovered. The control implementation circuit is designed. The great inductance increment and the corresponding variable duty ratio bring about an obvious decrement of the peak and RMS currents of power components, leading to a higher efficiency. Furthermore, the output voltage ripple is reduced and the PF is increased, especially at high input voltages.

Appendix

See Tables III–VII.

TABLE III
Optimum Harmonics Amounts and Boundary Inductance (μH) Without a Limited PF at $V_o = 400$ V

α	I_3^*	I_5^*	PF	L_b	α	I_3^*	I_5^*	PF	L_b	α	I_3^*	I_5^*	PF	L_b
0.32	0.0710	0.0065	0.9974	248	0.53	0.1562	0.0145	0.9879	512	0.74	0.3247	0.0305	0.9507	672
0.33	0.0743	0.0070	0.9972	260	0.54	0.1617	0.0150	0.9870	523	0.75	0.3368	0.0315	0.9472	674
0.34	0.0776	0.0075	0.9969	273	0.55	0.1673	0.0155	0.9861	534	0.76	0.3488	0.0320	0.9437	676
0.35	0.0806	0.0075	0.9967	286	0.56	0.1731	0.0160	0.9852	545	0.77	0.3630	0.0340	0.9395	677
0.36	0.0841	0.0080	0.9964	299	0.57	0.1796	0.0170	0.9841	556	0.78	0.3773	0.0355	0.9351	677
0.37	0.0872	0.0080	0.9961	312	0.58	0.1852	0.0170	0.9831	566	0.79	0.3927	0.0375	0.9302	677
0.38	0.0909	0.0085	0.9958	325	0.59	0.1921	0.0180	0.9818	575	0.80	0.4079	0.0385	0.9253	676
0.39	0.0946	0.0090	0.9955	338	0.60	0.1986	0.0185	0.9806	585	0.81	0.4244	0.0400	0.9199	674
0.40	0.0979	0.0090	0.9952	351	0.61	0.2059	0.0195	0.9792	594	0.82	0.4417	0.0415	0.9140	672
0.41	0.1019	0.0095	0.9948	364	0.62	0.2129	0.0200	0.9778	603	0.83	0.4594	0.0425	0.9080	669
0.42	0.1059	0.0100	0.9943	377	0.63	0.2201	0.0205	0.9764	611	0.84	0.4797	0.045	0.9008	665
0.43	0.1100	0.0105	0.9939	390	0.64	0.2281	0.0215	0.9747	619	0.85	0.5000	0.0465	0.8936	661
0.44	0.1137	0.0105	0.9935	402	0.65	0.2353	0.0215	0.9732	626	0.86	0.5226	0.0490	0.8854	655
0.45	0.1180	0.0110	0.9930	415	0.66	0.2444	0.0230	0.9711	633	0.87	0.5460	0.0510	0.8768	649
0.46	0.1224	0.0115	0.9925	428	0.67	0.2527	0.0235	0.9692	640	0.88	0.5714	0.0535	0.8673	642
0.47	0.1264	0.0115	0.9920	440	0.68	0.2619	0.0245	0.9671	646	0.89	0.5983	0.0560	0.8571	634
0.48	0.1316	0.0125	0.9913	453	0.69	0.2703	0.0245	0.9650	652	0.90	0.6276	0.0590	0.8459	625
0.49	0.1358	0.0125	0.9908	465	0.70	0.2812	0.0265	0.9623	657	0.91	0.6589	0.0620	0.8339	616
0.50	0.1407	0.0130	0.9901	477	0.71	0.2914	0.0275	0.9597	661	0.92	0.6925	0.0650	0.8209	605
0.51	0.1458	0.0135	0.9894	489	0.72	0.3021	0.0285	0.9569	666	0.93	0.7275	0.0670	0.8074	594
0.52	0.1509	0.0140	0.9887	501	0.73	0.3132	0.0295	0.9539	669	0.94	0.7685	0.0720	0.7916	582

TABLE IV
Optimum Harmonics Amounts and Boundary Inductance (μH) With a Limited PF at $V_o = 400$ V

$PF_{min} = 0.9$				$PF_{min} = 0.91$				$PF_{min} = 0.92$				$PF_{min} = 0.93$			
α	I_3^*	I_5^*	L_b	α	I_3^*	I_5^*	L_b	α	I_3^*	I_5^*	L_b	α	I_3^*	I_5^*	L_b
0.85	0.483201	0.032934	657	0.83	0.454056	0.037640	669	0.81	0.424137	0.039777	674	0.80	0.394267	0.027505	673
0.86	0.483836	0.021693	640	0.84	0.454826	0.026775	658	0.82	0.425050	0.028407	668	0.81	0.394732	0.019740	664
0.87	0.484242	0.008808	621	0.85	0.455328	0.016125	642	0.83	0.425550	0.019536	656	0.82	0.395069	0.011113	652
0.88	0.484322	0	599	0.86	0.455594	0.004211	625	0.84	0.425892	0.009512	642	0.83	0.395222	0.001612	639
0.89	0.484322	0	562	0.87	0.455613	0	601	0.85	0.425998	0	626	0.84	0.395225	0	621
0.90	0.484322	0	523	0.88	0.455613	0	568	0.87	0.425998	0	570	0.86	0.395225	0	570
0.91	0.484322	0	481	0.89	0.455613	0	532	0.89	0.425998	0	505	0.88	0.395225	0	511
0.92	0.484322	0	437	0.90	0.455613	0	495	0.91	0.425998	0	432	0.90	0.395225	0	446
0.93	0.484322	0	391	0.92	0.455613	0	414	0.93	0.425998	0	351	0.92	0.395225	0	372
0.94	0.484322	0	342	0.94	0.455613	0	324	0.94	0.425998	0	307	0.94	0.395225	0	291
$PF_{min} = 0.94$				$PF_{min} = 0.95$				$PF_{min} = 0.96$				$PF_{min} = 0.97$			
α	I_3^*	I_5^*	L_b	α	I_3^*	I_5^*	L_b	α	I_3^*	I_5^*	L_b	α	I_3^*	I_5^*	L_b
0.77	0.361489	0.032550	677	0.75	0.327795	0.024159	673	0.71	0.290455	0.026558	661	0.67	0.249752	0.020883	640
0.78	0.362163	0.023911	674	0.76	0.328176	0.018268	669	0.72	0.290984	0.019943	663	0.68	0.250109	0.016052	643
0.79	0.362545	0.017173	666	0.77	0.328463	0.012053	663	0.73	0.291273	0.015148	662	0.69	0.250327	0.012189	645
0.80	0.362823	0.009658	657	0.78	0.328640	0.005384	657	0.74	0.291499	0.009888	659	0.70	0.250499	0.007902	645
0.81	0.362949	0.001356	647	0.82	0.328684	0	600	0.75	0.291635	0.004297	655	0.71	0.250601	0.003441	645
0.82	0.362951	0	632	0.85	0.328684	0	537	0.76	0.291666	0	650	0.77	0.250623	0	606
0.86	0.362951	0	541	0.89	0.328684	0	432	0.82	0.291666	0	569	0.83	0.250623	0	520
0.90	0.362951	0	423	0.92	0.328684	0	336	0.88	0.291666	0	436	0.89	0.250623	0	387
0.94	0.362951	0	277	0.94	0.328684	0	263	0.94	0.291666	0	249	0.94	0.250623	0	235

TABLE V
OPTIMUM HARMONICS AMOUNTS AND BOUNDARY INDUCTANCE (μH) WITHOUT A LIMITED PF AT $V_o = 390$ V

α	I_3^*	I_5^*	PF	L_b	α	I_3^*	I_5^*	PF	L_b	α	I_3^*	I_5^*	PF	L_b
0.33	0.0730	0.0068	0.9973	243	0.55	0.1670	0.0152	0.9862	508	0.77	0.3631	0.0341	0.9394	644
0.34	0.0774	0.0072	0.9969	260	0.56	0.1731	0.0160	0.9852	519	0.78	0.3772	0.0354	0.9351	644
0.35	0.0807	0.0076	0.9967	272	0.57	0.1794	0.0168	0.9841	528	0.79	0.3919	0.0367	0.9305	644
0.36	0.0838	0.0077	0.9964	284	0.58	0.1851	0.0169	0.9831	538	0.80	0.4077	0.0383	0.9254	643
0.37	0.0874	0.0082	0.9961	297	0.59	0.1921	0.0180	0.9818	547	0.81	0.4242	0.0398	0.9199	641
0.38	0.0909	0.0085	0.9958	309	0.60	0.1984	0.0183	0.9807	556	0.82	0.4416	0.0414	0.9141	639
0.39	0.0942	0.0086	0.9955	321	0.61	0.2057	0.0193	0.9793	565	0.83	0.4593	0.0424	0.9080	636
0.40	0.0982	0.0092	0.9951	334	0.62	0.2129	0.0200	0.9778	573	0.84	0.4797	0.0450	0.9008	633
0.41	0.1020	0.0096	0.9947	346	0.63	0.2203	0.0207	0.9763	581	0.85	0.4996	0.0461	0.8938	628
0.42	0.1058	0.0099	0.9944	358	0.64	0.2280	0.0214	0.9747	589	0.86	0.5226	0.0490	0.8854	623
0.43	0.1098	0.0103	0.9939	371	0.65	0.2353	0.0215	0.9732	596	0.87	0.5462	0.0512	0.8767	617
0.44	0.1139	0.0107	0.9935	383	0.66	0.2443	0.0229	0.9711	603	0.88	0.5715	0.0536	0.8672	610
0.45	0.1181	0.0111	0.9930	395	0.67	0.2529	0.0237	0.9692	609	0.89	0.5975	0.0552	0.8574	603
0.46	0.1224	0.0115	0.9925	407	0.68	0.2620	0.0246	0.9670	615	0.90	0.6275	0.0589	0.8459	595
0.47	0.1264	0.0115	0.9920	419	0.69	0.2714	0.0256	0.9647	620	0.91	0.6587	0.0618	0.8339	586
0.48	0.1314	0.0123	0.9914	431	0.70	0.2811	0.0264	0.9623	625	0.92	0.6924	0.0649	0.8209	576
0.49	0.1362	0.0128	0.9907	442	0.71	0.2905	0.0266	0.9599	629	0.93	0.7273	0.0668	0.8075	565
0.50	0.1404	0.0127	0.9902	454	0.72	0.3019	0.0283	0.9569	633	0.94	0.7686	0.0721	0.7915	553
0.51	0.1460	0.0137	0.9894	465	0.73	0.3131	0.0294	0.9539	636	0.95	0.8118	0.0761	0.7750	541
0.52	0.1505	0.0136	0.9887	476	0.74	0.3247	0.0305	0.9507	639	0.96	0.8583	0.0798	0.7574	527
0.53	0.1558	0.0141	0.9879	487	0.75	0.3369	0.0316	0.9472	641					
0.54	0.1619	0.0152	0.9870	498	0.76	0.3487	0.0319	0.9438	643					

TABLE VI
OPTIMUM HARMONICS AMOUNTS AND BOUNDARY INDUCTANCE (μH) WITH A LIMITED PF AT $V_o = 390$ V

$PF_{min} = 0.87$				$PF_{min} = 0.88$				$PF_{min} = 0.887$				$PF_{min} = 0.89$			
α	I_3^*	I_5^*	L_b	α	I_3^*	I_5^*	L_b	α	I_3^*	I_5^*	L_b	α	I_3^*	I_5^*	L_b
0.88	0.564745	0.047345	610	0.87	0.537971	0.043698	616	0.86	0.518628	0.045234	623	0.86	0.510848	0.038745	622
0.89	0.565851	0.031482	593	0.88	0.538940	0.029427	600	0.87	0.519670	0.031051	610	0.87	0.511648	0.026137	605
0.90	0.566538	0.014600	569	0.89	0.539558	0.014123	578	0.88	0.520308	0.017340	589	0.88	0.512171	0.012154	585
0.91	0.566726	0	545	0.90	0.539742	0	557	0.89	0.520594	0.001728	568	0.89	0.512315	0.000448	563
0.92	0.566726	0	495	0.91	0.539742	0	513	0.90	0.520597	0	535	0.90	0.512315	0	526
0.93	0.566726	0	443	0.93	0.539742	0	416	0.91	0.520597	0	492	0.91	0.512315	0	484
0.94	0.566726	0	388	0.94	0.539742	0	365	0.93	0.520597	0	400	0.93	0.512315	0	393
0.95	0.566726	0	330	0.95	0.539742	0	311	0.95	0.520597	0	298	0.95	0.512315	0	293
0.96	0.566726	0	270	0.96	0.539742	0	253	0.96	0.520597	0	243	0.96	0.512315	0	240
$PF_{min} = 0.90$				$PF_{min} = 0.91$				$PF_{min} = 0.92$				$PF_{min} = 0.93$			
α	I_3^*	I_5^*	L_b	α	I_3^*	I_5^*	L_b	α	I_3^*	I_5^*	L_b	α	I_3^*	I_5^*	L_b
0.85	0.483201	0.032934	625	0.83	0.454056	0.037640	636	0.81	0.424137	0.039777	642	0.80	0.394267	0.027505	641
0.86	0.483836	0.021693	610	0.84	0.454826	0.026775	625	0.82	0.425050	0.028407	636	0.81	0.394732	0.019740	632
0.87	0.484242	0.008808	594	0.85	0.455328	0.016125	612	0.83	0.425550	0.019536	625	0.82	0.395069	0.011113	623
0.88	0.484322	0	571	0.86	0.455594	0.004211	598	0.84	0.425892	0.009512	613	0.83	0.395222	0.001612	612
0.89	0.484322	0	535	0.88	0.455613	0	541	0.87	0.425998	0	543	0.86	0.395225	0	543
0.90	0.484322	0	498	0.90	0.455613	0	471	0.89	0.425998	0	481	0.90	0.395225	0	424
0.92	0.484322	0	416	0.92	0.455613	0	394	0.91	0.425998	0	411	0.92	0.395225	0	355
0.94	0.484322	0	328	0.94	0.455613	0	309	0.94	0.425998	0	293	0.94	0.395225	0	278
0.96	0.484322	0	227	0.96	0.455613	0	214	0.96	0.425998	0	203	0.96	0.395225	0	193

TABLE VII
EXTENDED RESULTS REGARDING DIFFERENT OUTPUT VOLTAGE, SWITCHING FREQUENCY, AND OUTPUT POWER

Input voltage	Output power	Switching frequency	Output voltage	Critical inductance	Minimum PF
90~264VAC/50Hz	120W	100kHz	390VDC	L_{b1}=50μH, L_{b2}=243μH	PF_{min1}=0.812, PF_{min2}=0.887
			400VDC	L_{b1}=92μH, L_{b2}=250μH	PF_{min1}=0.854, PF_{min2}=0.960
90~264VAC/50Hz	120W	200kHz	390VDC	L_{b1}=25μH, L_{b2}=122μH	PF_{min1}=0.812, PF_{min2}=0.887
			400VDC	L_{b1}=46μH, L_{b2}=125μH	PF_{min1}=0.854, PF_{min2}=0.960
90~264VAC/50Hz	240W	100kHz	390VDC	L_{b1}=25μH, L_{b2}=122μH	PF_{min1}=0.812, PF_{min2}=0.887
			400VDC	L_{b1}=46μH, L_{b2}=125μH	PF_{min1}=0.854, PF_{min2}=0.960

REFERENCES

[1] O. Garcia, J. A. Cobos, R. Prieto, P. Alou, and J. Uceda, "Single phase power factor correction: A survey," *IEEE Trans. Power Electron.*, vol. 18, no. 3, pp. 749–755, May 2003.

[2] M. M. Jovanovic and Y. Jang, "State-of-the-art, single-phase, active power-factor-correction techniques for high-power applications-an overview," *IEEE Trans. Ind. Electron.*, vol. 52, no. 3, pp. 701–708, Jun. 2005.

[3] B. Singh, S. Singh, A. Chandra, and K. Al-Haddad, "Comprehensive study of single-phase ac-dc power factor corrected converters with high-frequency isolation," *IEEE Trans. Ind. Inform.*, vol. 7, no. 4, pp. 540–555, Nov. 2011.

[4] Y. Kim, W. Sung and B. Lee, "Comparative performance analysis of high density and efficiency PFC topologies," *IEEE Trans. Power Electron.*, vol. 29, no. 6, pp. 2666–2679, Jun. 2014.

[5] M. Gotfryd, "Output voltage and power limits in boost power factor corrector operating in discontinuous inductor current mode," *IEEE Trans. Power Electron.*, vol. 15, no. 1, pp. 51–57, Jan. 2000.

[6] Z. Z. Ye and M. M. Jovanovic, "Implementation and performance evaluation of DSP-based control for constant-frequency discontinuous-conduction-mode boost PFC front end," *IEEE Trans. Ind. Electron.*, vol. 52, no. 1, pp. 98–107, Feb. 2005.

[7] K. Raggl, T. Nussbaumer, G. Doerig, J. Biela, and J. W. Kolar, "Comprehensive design and optimization of a high-power-density single-phase boost PFC," *IEEE Trans. Ind. Electron.*, vol. 56, no. 7, pp. 2574–2587, Jul. 2009.

[8] K. Yao, X. Ruan, X. Mao and Z. Ye, "Variable-duty-cycle control to achieve high input power factor for DCM boost PFC converter," *IEEE Trans. Ind. Electron.*, vol. 58, no. 5, pp. 1856–1865, May 2011.

[9] R. Dayal, S. Dwari, and L. Parsa, "Design and implementation of a direct ac–dc boost converter for low-voltage energy harvesting," *IEEE Trans. Ind. Electron.*, vol. 58, no. 6, pp. 2387–2396, Jun. 2011.

[10] X. Zhang and J. W. Spencer, "Analysis of boost PFC converters operating in the discontinuous conduction mode," *IEEE Trans. Power Electron.*, vol. 26, no. 12, pp. 3621–3628, Dec. 2011.

[11] Z. Chen, P. Yang, G. Zhou, J. Xu, and Z. Chen, "Variable duty cycle control for quadratic boost PFC converter," *IEEE Trans. Ind. Electron.*, vol. 63, no. 7, pp. 4222–4232, Jul. 2016.

[12] R. K. Tripathi, S. P. Das, and G. K. Dubey, "Mixed-mode operation of boost switch-mode rectifier for wide range of load variations," *IEEE Trans. Power Electron.*, vol. 17, no. 6, pp. 999–1009, Nov. 2002.

[13] K. De Gusseme, D. M. Van de Sype, A. P. M. Van den Bossche, and J. A. Melkebeek, "Digitally controlled boost power-factor-correction converters operating in both continuous and discontinuous conduction mode," *IEEE Trans. Ind. Electron.*, vol. 52, no. 1, pp. 88–97, Feb. 2005.

[14] K. De Gusseme, D. M. Van de Sype, A. P. M. Van den Bossche, and J. A. Melkebeek, "Input-current distortion of CCM boost PFC converters operated in DCM," *IEEE Trans. Ind. Electron.*, vol. 54, no. 2, pp. 858–865, Apr. 2007.

[15] F. Chen and D. Maksimović, "Digital control for improved efficiency and reduced harmonic distortion over wide load range in boost PFC rectifiers," *IEEE Trans. Power Electron.*, vol. 25, no. 10, pp. 2683–2692, Oct. 2010.

[16] S. F. Lim and A. M. Khambadkone, "A simple digital DCM control scheme for boost PFC operating in both CCM and DCM," *IEEE Trans. Ind. Appl.*, vol. 47, no. 4, pp. 1802–1812, Jul./Aug. 2011.

[17] S. Moon, L. Corradini, and D. Maksimović, "Autotuning of digitally controlled boost power factor correction rectifiers," *IEEE Trans. Power Electron.*, vol. 26, no. 10, pp. 3006–3018, Oct. 2011.

[18] C. W. Clark, F. Musavi, and W. Eberle, "Digital DCM detection and mixed conduction mode control for boost PFC converters," *IEEE Trans. Power Electron.*, vol. 29, no. 1, pp. 347–355, Jan. 2014.

[19] Q. Ji, X. Ruan, L. Xie and Z. Ye, "Conducted EMI spectra of average-current-controlled boost PFC converters operating in both CCM and DCM," *IEEE Trans. Ind. Electron.*, vol. 62, no. 4, pp. 2184–2194, Apr. 2015.

[20] R. Fernandes and O. Trescases, "A multimode 1-MHz PFC front end with digital peak current modulation," *IEEE Trans. Power Electron.*, vol. 31, no. 8, pp. 5694–5708, Aug. 2016.

[21] H. Youn, J. Lee, J. Baek, and G. Moon, "A digital phase leading filter current compensation (PLFCC) technique for CCM boost PFC converter to improve PF in high line voltage and light load conditions," *IEEE Trans. Power Electron.*, vol. 31, no. 9, pp. 6596–6606, Sep. 2016.

Kai Yao (M'14) was born in Jiangsu Province, China, in 1980. He received the B.S. degree in industrial automation from Nantong University, Nantong, China, the M.S. degree in mechanical design and theory, and the Ph.D. degree in electrical engineering from the Nanjing University of Aeronautics and Astronautics, Nanjing, China, in 2002, 2005, and 2010 respectively.

In 2011, he joined the Faculty of Electrical Engineering, School of Automation, Nanjing University of Science and Technology, where he has been engaged in teaching and research in the field of power electronics. His main research interests include power factor correction converters, condition monitoring, and diagnostics of power converters.

Lei Li was born in Anhui Province, China, in 1993. He received the B.S. degree in electrical engineering and automation from the Nanjing University of Science and Technology, Nanjing, China, in 2016. He is currently pursuing the M.S. degree in power electronics and electric drives from the same University.

His research interest includes power factor correction converters.

Huanqi Tang was born in Sichuan, China, in 1994. He received the B.S. degree in smart grid and information engineering from the Nanjing University of Science and Technology, Nanjing, China, in 2016. He is currently pursuing the M.S. degree in power electronics from the same University.

His research interest includes power factor correction converters.

Chunyan Mao was born in Jiangsu, China, in 1994. She received the B.S. degree in electrical engineering and automation from Nanjing Normal University, Nanjing, China, in 2016. She is currently pursuing the M.S. degree in electrical engineering from the Nanjing University of Science and Technology, Nanjing.

Her research interests include power factor correction converters and capacitance monitoring technology.

Kaili Chen was born in Jiangsu, China, in 1994. He received the B.S. degree in smart grid and information engineering from the Nanjing University of Science and Technology, Nanjing, China, in 2016. He is currently pursuing the M.S. degree in power electronics from the same University.

His research interest includes power factor correction converters.